Biomedical Optics EXPRESS

A high-efficiency fiber-based imaging system for co-registered autofluorescence and optical coherence tomography

Hamid Pahlevaninezhad,[1] Anthony M. D. Lee,[1] Tawimas Shaipanich,[1] Rashika Raizada,[1] Lucas Cahill,[1] Geoffrey Hohert,[1] Victor X. D. Yang,[2] Stephen Lam,[1] Calum MacAulay,[1] and Pierre Lane[1*]

[1]*Integrative Oncology Department—Imaging Unit, BC Cancer Research Center, 675 West 10th Avenue, Vancouver, Canada*

[2]*Biophotonics and Bioengineering Laboratory, Electrical and Computer Engineering, Ryerson University, Toronto, ON, Canada*

[*]*plane@bccrc.ca*

Abstract: We present a power-efficient fiber-based imaging system capable of co-registered autofluorescence imaging and optical coherence tomography (AF/OCT). The system employs a custom fiber optic rotary joint (FORJ) with an embedded dichroic mirror to efficiently combine the OCT and AF pathways. This three-port wavelength multiplexing FORJ setup has a throughput of more than 83% for collected AF emission, significantly more efficient compared to previously reported fiber-based methods. A custom 900 μm diameter catheter – consisting of a rotating lens assembly, double-clad fiber (DCF), and torque cable in a stationary plastic tube – was fabricated to allow AF/OCT imaging of small airways *in vivo*. We demonstrate the performance of this system *ex vivo* in resected porcine airway specimens and *in vivo* in human on fingers, in the oral cavity, and in peripheral airways.

OCIS codes: (110.0110) Imaging systems; (110.2350) Fiber optics imaging; (110.4500) Optical coherence tomography; (170.2520) Fluorescence microscopy; (170.3890) Medical optics instrumentation.

References and links

1. S. Lam, T. Kennedy, M. Unger, Y. E. Miller, D. Gelmont, V. Rusch, B. Gipe, D. Howard, J. C. LeRiche, A. Coldman, and A. F. Gazdar, "Localization of bronchial intraepithelial neoplastic lesions by fluorescence bronchoscopy," Chest **113**(3), 696–702 (1998).
2. T. C. Kennedy, S. Lam, and F. R. Hirsch, "Review of recent advances in fluorescence bronchoscopy in early localization of central airway lung cancer," Oncologist **6**(3), 257–262 (2001).
3. J. Hung, S. Lam, J. C. LeRiche, and B. Palcic, "Autofluorescence of normal and malignant bronchial tissue," Lasers Surg. Med. **11**(2), 99–105 (1991).
4. B. J. Venmans, H. van der Linden, T. J. van Boxem, P. E. Postmus, E. F. Smit, and T. G. Sutedja, "Early detection of pre-invasive lesions in high risk patients. A comparison of conventional fiber optic and fluorescence bronchoscopy," J. Bronchoscopy **5**(4), 280–283 (1998).
5. D. Huang, E. A. Swanson, C. P. Lin, J. S. Schuman, W. G. Stinson, W. Chang, M. R. Hee, T. Flotte, K. Gregory, C. A. Puliafito, and J. G. Fujimoto, "Optical Coherence Tomography," Science **254**(5035), 1178–1181 (1991).
6. J. G. Fujimoto, M. E. Brezinski, G. J. Tearney, S. A. Boppart, B. Bouma, M. R. Hee, J. F. Southern, and E. A. Swanson, "Optical biopsy and imaging using optical coherence tomography," Nat. Med. **1**(9), 970–972 (1995).
7. G. J. Tearney, M. E. Brezinski, B. E. Bouma, S. A. Boppart, C. Pitris, J. F. Southern, and J. G. Fujimoto, "In vivo endoscopic optical biopsy with optical coherence tomography," Science **276**(5321), 2037–2039 (1997).
8. M. Tsuboi, A. Hayashi, N. Ikeda, H. Honda, Y. Kato, S. Ichinose, and H. Kato, "Optical coherence tomography in the diagnosis of bronchial lesions," Lung Cancer **49**(3), 387–394 (2005).
9. S. Lam, B. Standish, C. Baldwin, A. McWilliams, J. leRiche, A. Gazdar, A. I. Vitkin, V. Yang, N. Ikeda, and C. MacAulay, "In vivo optical coherence tomography imaging of preinvasive bronchial lesions," Clin. Cancer Res. **14**(7), 2006–2011 (2008).

#214233 - $15.00 USD Received 20 Jun 2014; revised 31 Jul 2014; accepted 1 Aug 2014; published 6 Aug 2014

10. H. Pahlevaninezhad, I. Cecic, A. M. D. Lee, A. H. Kyle, S. Lam, C. MacAulay, and P. M. Lane, "Multimodal tissue imaging: using coregistered optical tomography data to estimate tissue autofluorescence intensity change due to scattering and absorption by neoplastic epithelial cells," J. Biomed. Opt. **18**(10), 106007 (2013).
11. J. K. Barton, F. Guzman, and A. Tumlinson, "Dual modality instrument for simultaneous optical coherence tomography imaging and fluorescence spectroscopy," J. Biomed. Opt. **9**(3), 618–623 (2004).
12. S. Yuan, Q. Li, J. Jiang, A. Cable, and Y. Chen, "Three-dimensional coregistered optical coherence tomography and line-scanning fluorescence laminar optical tomography," Opt. Lett. **34**(11), 1615–1617 (2009).
13. S. Yuan, C. A. Roney, J. Wierwille, C. W. Chen, B. Xu, G. Griffiths, J. Jiang, H. Ma, A. Cable, R. M. Summers, and Y. Chen, "Co-registered optical coherence tomography and fluorescence molecular imaging for simultaneous morphological and molecular imaging," Phys. Med. Biol. **55**(1), 191–206 (2010).
14. J. Park, J. A. Jo, S. Shrestha, P. Pande, Q. Wan, and B. E. Applegate, "A dual-modality optical coherence tomography and fluorescence lifetime imaging microscopy system for simultaneous morphological and biochemical tissue characterization," Biomed. Opt. Express **1**(1), 186–200 (2010).
15. Y. Chen, S. Yuan, J. Wirewille, R. Naphas, Q. Li, T. R. Blackwell, P. T. Winnard, Jr., V. Raman, and K. Glunde, "Integrated optical coherence tomography (OCT) and fluorescence laminar optical tomography (FLOT)," IEEE J. Sel. Top. Quantum Electron. **16**(4), 755–766 (2010).
16. M. Gaertner, P. Cimalla, L. Knels, S. Meissner, C. Schnabel, W. M. Kubler, and E. Koch, "Investigation of alveolar tissue deformations using OCT combined with fluorescence microscopy," Proc. SPIE **8091**, Optical Coherence Tomography and Coherence Techniques **V**, 80911P (2011).
17. J. Y. Qu, Z. Huang, and J. Hua, "Excitation-and-collection geometry insensitive fluorescence imaging of tissue-simulating turbid media," Appl. Opt. **39**(19), 3344–3356 (2000).
18. R. J. McNichols, A. Gowda, B. A. Bell, R. M. Johnigan, K. H. Calhoun, and M. Motamedi, "Development of an endoscopic fluorescence image guided OCT probe for oral cancer detection," Proc. SPIE **4254**, 23–30 (2001).
19. Y. T. Pan, T. Q. Xie, C. W. Du, S. Bastacky, S. Meyers, and M. L. Zeidel, "Enhancing early bladder cancer detection with fluorescence-guided endoscopic optical coherence tomography," Opt. Lett. **28**(24), 2485–2487 (2003).
20. A. R. Tumlinson, L. P. Hariri, U. Utzinger, and J. K. Barton, "A miniature endoscope for simultaneous OCT-LIF measurement," Appl. Opt. **43**(1), 113–121 (2004).
21. L. P. Hariri, A. R. Tumlinson, D. G. Besselsen, U. Utzinger, E. W. Gerner, and J. K. Barton, "Endoscopic optical coherence tomography and laser-induced fluorescence spectroscopy in a murine colon cancer model," Lasers Surg. Med. **38**(4), 305–313 (2006).
22. R. A. Wall, G. T. Bonnema, and J. K. Barton, "Novel focused OCT-LIF endoscope," Biomed. Opt. Express **2**(3), 421–430 (2011).
23. A. M. Winkler, P. F. Rice, J. Weichsel, J. M. Watson, M. V. Backer, J. M. Backer, and J. K. Barton, "In vivo, dual-modality OCT/LIF imaging using a novel VEGF receptor-targeted NIR fluorescent probe in the AOM-treated mouse model," Mol. Imaging Biol. **13**(6), 1173–1182 (2011).
24. A. M. Fard, P. Vacas-Jacques, E. Hamidi, H. Wang, R. W. Carruth, J. A. Gardecki, and G. J. Tearney, "Optical coherence tomography--near infrared spectroscopy system and catheter for intravascular imaging," Opt. Express **21**(25), 30849–30858 (2013).
25. S. Tang, T. B. Krasieva, Z. Chen, and B. J. Tromberg, "Combined multiphoton microscopy and optical coherence tomography using a 12-fs broadband source," J. Biomed. Opt. **11**(2), 020502 (2006).
26. A. R. Tumlinson, J. K. Barton, B. Považay, H. Sattman, A. Unterhuber, R. A. Leitgeb, and W. Drexler, "Endoscope-tip interferometer for ultrahigh resolution frequency domain optical coherence tomography in mouse colon," Opt. Express **14**(5), 1878–1887 (2006).
27. M. T. Myaing, D. J. MacDonald, and X. Li, "Fiber-optic scanning two-photon fluorescence endoscope," Opt. Lett. **31**(8), 1076–1078 (2006).
28. S. Tang, W. Jung, D. McCormick, T. Xie, J. Su, Y. C. Ahn, B. J. Tromberg, and Z. Chen, "Design and implementation of fiber-based multiphoton endoscopy with microelectromechanical systems scanning," J. Biomed. Opt. **14**(3), 034005 (2009).
29. S. Tang, Y. Zhou, K. K. H. Chan, and T. Lai, "Multiscale multimodal imaging with multiphoton microscopy and optical coherence tomography," Opt. Lett. **36**(24), 4800–4802 (2011).
30. G. Liu and Z. Chen, "Fiber-based combined optical coherence and multiphoton endomicroscopy," J. Biomed. Opt. **16**(3), 036010 (2011).
31. K. Murari, Y. Zhang, S. Li, Y. Chen, M. J. Li, and X. Li, "Compensation-free, all-fiber-optic, two-photon endomicroscopy at 1.55 μm," Opt. Lett. **36**(7), 1299–1301 (2011).
32. C. Dai, X. Liu, and S. Jiao, "Simultaneous optical coherence tomography and autofluorescence microscopy with a single light source," J. Biomed. Opt. **17**(8), 080502 (2012).
33. S. Y. Ryu, H. Y. Choi, J. Na, E. S. Choi, and B. H. Lee, "Combined system of optical coherence tomography and fluorescence spectroscopy based on double-cladding fiber," Opt. Lett. **33**(20), 2347–2349 (2008).
34. H. Bao, S. Y. Ryu, B. H. Lee, W. Tao, and M. Gu, "Nonlinear endomicroscopy using a double-clad fiber coupler," Opt. Lett. **35**(7), 995–997 (2010).
35. S. Lemire-Renaud, M. Rivard, M. Strupler, D. Morneau, F. Verpillat, X. Daxhelet, N. Godbout, and C. Boudoux, "Double-clad fiber coupler for endoscopy," Opt. Express **18**(10), 9755–9764 (2010).

#214233 - $15.00 USD Received 20 Jun 2014; revised 31 Jul 2014; accepted 1 Aug 2014; published 6 Aug 2014

36. S. Liang, A. Saidi, J. Jing, G. Liu, J. Li, J. Zhang, C. Sun, J. Narula, and Z. Chen, "Intravascular atherosclerotic imaging with combined fluorescence and optical coherence tomography probe based on a double-clad fiber combiner," J. Biomed. Opt. **17**(7), 070501 (2012).
37. J. Mavadia, J. Xi, Y. Chen, and X. Li, "An all-fiber-optic endoscopy platform for simultaneous OCT and fluorescence imaging," Biomed. Opt. Express **3**(11), 2851–2859 (2012).
38. D. Yelin, B. E. Bouma, S. H. Yun, and G. J. Tearney, "Double-clad fiber for endoscopy," Opt. Lett. **29**(20), 2408–2410 (2004).
39. L. Wang, H. Y. Choi, Y. Jung, B. H. Lee, and K. T. Kim, "Optical probe based on double-clad optical fiber for fluorescence spectroscopy," Opt. Express **15**(26), 17681–17689 (2007).
40. D. Lorenser, B. C. Quirk, M. Auger, W. J. Madore, R. W. Kirk, N. Godbout, D. D. Sampson, C. Boudoux, and R. A. McLaughlin, "Dual-modality needle probe for combined fluorescence imaging and three-dimensional optical coherence tomography," Opt. Lett. **38**(3), 266–268 (2013).
41. T. Chen, N. Zhang, T. Huo, C. Wang, J. G. Zheng, T. Zhou, and P. Xue, "Tiny endoscopic optical coherence tomography probe driven by a miniaturized hollow ultrasonic motor," J. Biomed. Opt. **18**(8), 086011 (2013).
42. W. J. Madore, E. De Montigny, O. Ouellette, S. Lemire-Renaud, M. Leduc, X. Daxhelet, N. Godbout, and C. Boudoux, "Asymmetric double-clad fiber couplers for endoscopy," Opt. Lett. **38**(21), 4514–4517 (2013).
43. H. Pahlevaninezhad, A. M. D. Lee, S. Lam, C. MacAulay, and P. M. Lane, "Coregistered autofluorescence-optical coherence tomography imaging of human lung sections," J. Biomed. Opt. **19**(3), 036022 (2014).

1. Introduction

Compared to white-light bronchoscopy, autofluorescence (AF) bronchoscopy has been shown to be up to 6 times more sensitive in detecting intraepithelial neoplastic lesions in the lung [1–4] by allowing visualization of biochemical changes in tissue. Optical coherence tomography (OCT) [5–7] provides structural information millimeters deep into the tissue with about 10 μm axial resolution. OCT can be used to study high-risk tissue sites without performing biopsies and tissue removal [8]. Our group has previously shown that bronchial epithelial thickness measured by OCT correlates with pathological grade [9]. When used in combination, AF/OCT imaging can provide biochemical information co-localized with structural information, potentially enabling increased diagnostic sensitivity and specificity. For example, a combined AF/OCT system could quantify the fraction of AF loss due to collagen remodeling in the stroma by removing the fraction of AF loss due to epithelial scattering and absorption (attenuation) from the measured AF signal [10]. Additionally, co-localized AF/OCT may be of particular importance in the lung where commercial endoscopes allow wide-field AF imaging in the central airways but cannot be extended to the peripheral airways due to size constraints.

OCT systems are typically designed to operate in the near infrared wavelength range where there is a good balance between tissue penetration and resolution. However, AF imaging systems are designed with visible or UV light sources to access biologically relevant fluorophores. Thus, optical components capable of operating at these two very different wavelength ranges are required to combine the two modalities. Several groups have published methods for combining OCT and AF imaging using free space optical components and dichroic mirrors [11–16]. For endoscopic imaging such as in lung, the need for fiber optic catheters creates additional challenges. Fiber-based catheters that use separate adjacent fibers for the two modalities have been developed [17–24]. However, this approach compromises co-registration of the two modalities. Other reported approaches have used single Ti-Sapphire broadband femtosecond (fs) laser sources for both spectral domain OCT and multiphoton excited fluorescence imaging systems [25–32]. Double-clad fiber (DCF) can also provide a common path for the two modalities that ensures co-registration. Additionally, DCF has relatively high AF collection efficiency due to the large inner cladding [33–40].

Endoscopic imaging of cylindrical structures such as airways favors fiber optic probes that scan in a rotational manner using proximal or distal motors. In the distal scanning case, the catheter commonly includes a stationary fiber and a distally located micromotor that actuates a rotating mirror [36, 37]. However, using micromotors increases the overall catheter diameter and creates blind sectors due to wiring. Miniaturized ultrasonic actuators have also been reported free from blind sectors [41]. In the proximal scanning case, a large-scale motor

#214233 - $15.00 USD Received 20 Jun 2014; revised 31 Jul 2014; accepted 1 Aug 2014; published 6 Aug 2014

actuates the rotor of a fiber optic rotary joint (FORJ) that is connected to an imaging catheter that consists of optical fiber and distal beam shaping optics. For our work, we have chosen proximal scanning to ease catheter miniaturization. In addition, as motor components are separated from the catheter, proximally actuated catheters can be less complicated and less expensive to manufacture.

There are three challenges to implementing a DCF-based AF/OCT system: 1) combining the blue AF excitation light and incident OCT light; 2) separating the green AF emission from the back-scattered OCT light; and 3) designing a broadband FORJ capable of supporting the broad wavelength range of the two imaging modalities. The first two challenges have been addressed by other researchers using wavelength division multiplexers (WDMs). Commercially available WDMs with close input wavelengths ranges (635 nm/1310 nm) have been employed [33, 36, 40] albeit with a low AF excitation power transmission efficiency (~23%). Custom designed WDMs have shown enhanced blue AF excitation power efficiency (~60%) [37]. DCF couplers and (2 + 1):1 pump/signal DCF combiners have been proposed for splitting green AF emission from the back-scattered OCT light [30, 33–36, 40] with 42% [35, 40] and 20% [30, 36] collection of AF emissions, respectively. Asymmetric DCF couplers have been recently developed with significantly increased coupling of inner-cladding light (70%) that can be used for extracting AF emissions [42]. However, any solution using WDMs will also require an FORJ and imaging catheter that will introduce additional losses for AF emissions. In this work, we present a custom-designed FORJ and associated free-space optical assembly that efficiently addresses all three challenges simultaneously. This system has power efficiency for collected AF emissions greater than previously demonstrated methods. We couple this system to a custom built small diameter rotating DCF-based catheter suitable for *in vivo* small airway AF/OCT imaging.

2. Materials and methods

The AF/OCT imaging system is shown in Fig. 1. The two key components in this dual-modality imaging system are a specially designed three-port FORJ with an embedded dichroic mirror and a custom 900 μm diameter DCF-based catheter. The three-port FORJ efficiently combine the OCT and AF pathways and the DCF-based catheter allows high AF collection efficiency due to the large inner cladding.

OCT Imaging: The OCT subsystem includes a 50.4 kHz wavelength-swept laser source (SSOCT-1310, Axsun Technologies Inc., Billerica, MA, USA) with 20 mW output power centered at 1310 nm with 100 nm bandwidth (FWHM). This laser source drives a fiber-based Mach-Zehnder interferometer with reference and sample arms, as shown in Fig. 1 (OCT inset). The interference is detected by a balanced photodetector (PDB420A, ThorLabs, Newton, NJ, USA) whose output is fed into one channel of a digitizer card (ATS9350, AlazarTech, Pointe-Claire, QC, Canada).

AF Imaging: The AF imaging subsystem uses a 445 nm semiconductor laser (CUBE 445-40C, Coherent, Santa Clara, CA, USA) as the excitation source. It is coupled to the FORJ dichroic mirror using free-space optics to provide about 7 mW of optical power to the sample after the DCF catheter. A dichroic beamsplitter (DM_2) (ZT442rdc-1, Chroma, Bellows Falls, VT, USA) and an emission filter (E480LPXT, Chroma, Bellows Falls, VT, USA) separate back-scattered blue AF excitation light from AF photons as shown in Fig. 1 (AF inset). The collected AF emission is detected by a PMT detector module (H9433-201, Hamamatsu, Japan) whose output is fed into the second channel of the digitizer card.

Three-port FORJ: The AF and OCT modalities are combined using the specially designed three-port FORJ with an embedded dichroic mirror. This custom FORJ was designed to our specifications and supplied by Princetel Inc. (Pennington, NJ). The stator of the three-port FORJ consists of a single mode fiber (SMF) port that is collimated by a stationary rod lens L_1 (f = 3 mm, BK-7). An anti-reflection coated long-pass dichroic mirror DM_1 (FF875-Di01-5 × 5, Semrock, Rochester, NY, USA) is mounted at 45° in the infinity space within the FORJ

#214233 - $15.00 USD Received 20 Jun 2014; revised 31 Jul 2014; accepted 1 Aug 2014; published 6 Aug 2014

body. The FORJ rotor consists of a second rod lens L_2 (f = 3 mm, BK-7) that couples to a DCF port. The infrared (IR) OCT light path through the FORJ is from the SMF port to the core of the DCF port. A free-space port on the three-port FORJ allows visible AF excitation and emission beams to be coupled to and from the inner cladding of the DCF port. Both rod lenses are cut at 8° to minimize back-reflection and L_1 has IR anti-reflection coating to minimize insertion loss. L_2 does not have any anti-reflection coating so that it can support both visible and IR wavelength ranges. To maintain high coupling efficiency during the rotation for FORJ, it is important that the optical axis of L_2 is aligned with the rotor axis. All other optical components must be aligned around this constraint to achieve maximum power throughput.

The insertion losses of the three-port FORJ were measured to be 0.5 dB, 2.0 dB, and 0.8 dB at OCT (1310 nm), blue (445 nm), and green (550 nm) wavelengths, respectively. The insertion loss at 1310 nm was measured as the ratio of optical power detected from the core of the DCF pigtail to that coupled into the SMF pigtail. Insertion losses for the two AF pathways were measured by coupling light into the inner cladding of the DCF pigtail and measuring the power emitted at the free-space port. Blue and green light was first coupled into the inner cladding of a DCF patch cable (coupling into the inner cladding was confirmed by imaging). The DCF patch cable was then connected to the DCF pigtail to couple light into the FORJ. Insertion loss was measured as the ratio of optical power detected at the free-space port of the FORJ to that delivered from the DCF patch cable. Insertion loss at 550 nm was measured to approximate AF emission losses. Since AF emissions are usually weak, it is important to minimize losses for the AF light. The FORJ is mounted on a custom built motor assembly that allows rotational and pullback imaging capability. The moving parts in the rotary pullback drive (RPD) during pullback are distinguished by the dashed black line in Fig. 1.

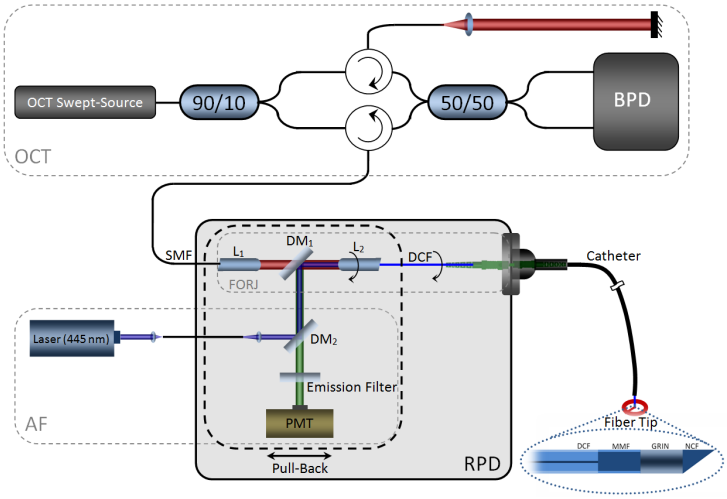

Fig. 1. AF/OCT imaging system; L: lens, DM: dichroic mirror; PMT: photomultiplier; FORJ: fiber optic rotary joint; RPD: rotary pull-back drive; DCF: Double-clad fiber; BPD: balanced photo-detector, Fiber Tip inset; DCF: double-clad fiber; MMF: multi-mode fiber; GRIN: graded index fiber; NCF: no-core fiber.

Custom data acquisition software acquires the AF and OCT data and provides immediate AF and OCT display. The AF and OCT data streams are read simultaneously by a digitizer using the k-clock from the OCT laser ensuring registration of the AF and OCT data. As no depth information is encoded in the AF stream each AF data point is averaged over the length of the OCT A-line.

Catheter: For *in vivo* AF/OCT imaging we developed a DCF-based fiber optic assembly consisting of a 1.5 m-long length of DCF (9/105/125-20PI, FUD-3489, Nufern, East Granby,

#214233 - $15.00 USD Received 20 Jun 2014; revised 31 Jul 2014; accepted 1 Aug 2014; published 6 Aug 2014

CT, USA) (NA_{core} = 0.12; $NA_{inner\ cladding}$ = 0.22) spliced to beam-shaping fiber optics, illustrated in Fig. 1 (fiber tip inset). The beam-shaping optics consists of a 450 μm-long step-index multimode fiber (MMF) (MM-S105/125-22A, Nufern, East Granby, CT, USA), a 65 μm-long graded-index fiber (GRIN) (GIF625, ThorLabs, Newton, NJ, USA), and an angle-polished no-core fiber (NCF) (NDF125, POFC Optical Fiber, Taiwan). The MMF with large core diameter allows expansion of the forward-going OCT beam to increase the numerical aperture of the following focusing lens and, in turn, provide high lateral resolution for OCT imaging with long working distance. The length of this section is designed such that the OCT light does not expand to reach the MMF cladding. However, for AF imaging, the MMF confines light that is originally travelling within the DCF large inner cladding, enhancing the power throughput of both the blue AF excitation light and the collected AF emission. The GRIN segment focuses the blue AF excitation and OCT beams on the sample and the angle-polished NCF total internally reflects the beams at approximately 63° from the fiber axis to the side of the fiber-optic assembly. The fiber assembly is fixed inside a torque cable that transfers rotational motion from the RPD to the distal end. This rotating assembly is placed inside a 900 μm diameter open-ended stationary plastic tube. The spot size of the DCF fiber-optic assembly was measured to be $[2w_{0x}, 2w_{0y}]$ = [16 μm, 24μm] and [53 μm, 60 μm] at 1310 nm and 445 nm, respectively, with 750 μm ± 50 μm working distance measured from the end of the GRIN segment. Due to the large diameter of the DCF inner cladding, the blue AF excitation light is multimode. However, as numerous modes are excited, the emitted AF excitation is approximately Gaussian with [53 μm, 60 μm] lateral mode field diameters.

We used the AF/OCT imaging system for *in vivo* imaging of human finger pads, oral cavity, and *ex vivo* pig airways with the AF/OCT catheter's fiber assembly rotating at 5 Hz and over 10 mm pullback length with 0.2 mm/s pullback speed. AF/OCT imaging of the finger pads was carried out with two fingers holding the stationary plastic tube at the distal end of the catheter. Oral imaging was performed by placing the catheter inside a volunteer's oral cavity with the end of the catheter located at the tip of the tongue so that tongue, teeth, and lips were covered over the length of the 10 mm pullback. The lips were closed during oral cavity imaging. For porcine imaging, a fresh whole lung was harvested from a Yucatan miniature pig immediately following euthanization. The donation of animal tissue was approved by the institutional review board at the University of British Columbia (A11-0374). The AF/OCT catheter was inserted through the trachea and pushed forward until it reached an airway that had a luminal diameter approximately equal to that of the catheter.

The AF/OCT imaging system was also used for *in vivo* human lung imaging. In this case, a sterilized 1.5 mm diameter closed ended sheath was used over the open-ended plastic tube to prevent direct catheter-patient contact. A bronchoscope guided the OCT probe to normal airways determined by CT-scan prior to the imaging. *In vivo* human lung imaging was approved by the Research Ethics Board of the University of British Columbia and the British Columbia Cancer Agency (H14-00695). The subject provided written consent.

3. Results and discussion

The three-dimensional point spread function (PSF) of the AF imaging modality was measured to assess its resolution. We constructed a phantom of blue fluorescent microspheres (0.03 mL, 2.1 μm diameter, 1% solids, catalogue number B0200, Thermo Scientific, Fermont, CA) embedded in a silicone elastomer matrix (5.5 mL Sylgard 184, Corning Corporation, Midland, MI). To ensure a uniform mixture, the solution was stirred manually and then placed in an ultrasonic water bath for 30 minutes. A close-ended plastic sheath was immersed in the solution to accommodate the DCF assembly. Finally, the solution was cured over 50°C heat for 5 hours. The phantom was imaged with the AF/OCT imaging system over a 10 mm pullback. As illustrated in Fig. 2(b), microsphere distance from the catheter axis was determined from OCT while the PSF of the AF modality was obtained by measuring the full width at half maximum (FWHM) of the sphere's impulse response. As the AF/OCT imaging

#214233 - $15.00 USD Received 20 Jun 2014; revised 31 Jul 2014; accepted 1 Aug 2014; published 6 Aug 2014

catheter spins, OCT images are collected in polar coordinates where r is the A-line depth coordinate and θ is the azimuthal coordinate. The z coordinate is the pullback dimension. The FWHM measured along the two orthogonal scanning directions (θ and z) as a function of radial distance from the catheter is plotted in Fig. 2(a). Assuming a Gaussian-like beam and PSF, the measured FWHM data was fit to a hyperbola to model its dependence on axial position.

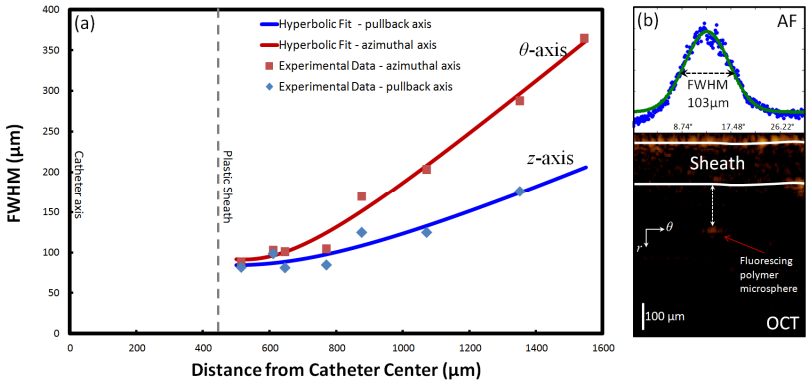

Fig. 2. AF lateral point spread function (PSF); (a) the FWHM measured along θ and z axis versus the distance from the catheter axis for the AF imaging system obtained from AF and OCT imaging of microspheres in silicone, (b) co-registered AF/OCT imaging of a microsphere.

Due to the fiber assembly optics, the AF excitation and detection efficiency is dependent upon the distance of the sample from the fiber assembly. To characterize the AF signal attenuation as a function of distance, we conducted an experiment with a fluorescent-slide phantom and varied the phantom-catheter distance while recording the relative AF signal intensity. Figure 3 shows the normalized AF signal with respect to the distance from the catheter axis.

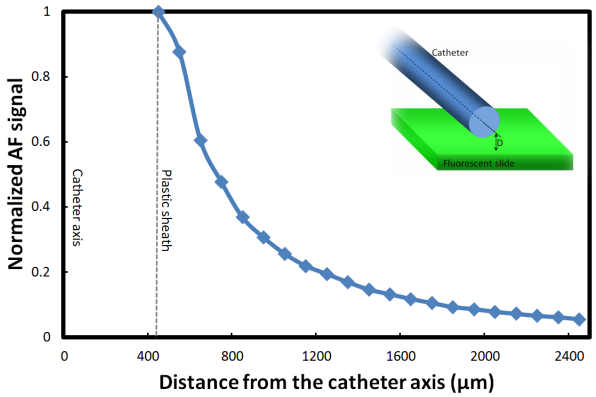

Fig. 3. AF signal attenuation vs. sample-catheter distance; normalized AF signal amplitudes corresponding to different fluorescent slide-catheter distance.

The detection sensitivity of AF imaging is limited by either not-fully-suppressed back-scattered blue AF excitation light or background AF generated in the catheter and/or FORJ components of the excitation pathway. It is difficult to determine with certainty which effect limits the sensitivity because the two noise sources cannot be removed independently. Nevertheless, to obtain a rough estimation we measured the PMT noise floor for three cases: 1) when the blue AF excitation was blocked, 2) when the catheter was disconnected in the presence of blue AF excitation light, and 3) when the catheter was running in free space in the

#214233 - $15.00 USD Received 20 Jun 2014; revised 31 Jul 2014; accepted 1 Aug 2014; published 6 Aug 2014

presence of blue AF excitation light. The noise floor was the smallest for the first case as expected, increased by 9.3 dB in the presence of the blue AF excitation light with no catheter, and increased by 10.3 dB (compared to the first case) in the presence of the blue excitation light with the catheter running in free-space. Therefore, the catheter seems to have a small effect on the detection sensitivity and the detection sensitivity seems to be limited by the combination of not-fully-suppressed back-scattered blue AF excitation light and AF emission created in the FORJ components. We suspect that the reflection from L_2 is the main source of back-scattered blue AF excitation light since it has no anti-reflection coating.

The use of DCF-based catheters can create some artefacts in the OCT image. The problem arises from the fact that the back-scattered OCT light is collected by both the core and the inner cladding of the DCF. While light propagation in the core is single-mode, the fraction propagating in the inner cladding is multimode with a wide distribution of optical path lengths, creating broad ghost artefacts in the OCT image. Ideally, the FORJ would function like a perfect relay lens and couple the OCT back-scattered light from the DCF core into the SMF core and significantly suppress the coupling of inner cladding light. However, since the inner cladding is much larger than the core, the optical power collected by the DCF inner cladding is also much larger than the optical power collected by the core. Therefore, any small discontinuity such as connector mating can cross-couple a small fraction of the large unwanted inner cladding power into the core. A simple solution to remove these artefacts is to use a longer catheter. Given that the inner-cladding modes propagate slower than those of the core, a long catheter can push the artefacts created by the inner-cladding modes outside the OCT ranging depth.

In vivo and *ex vivo* imaging results are presented in Fig. 4 and Fig. 5. Figure 4 shows results from human fingers, human oral cavity, and porcine airways. The top row (polar coordinates) and the middle row (Cartesian coordinate) show the volumetric OCT images with the AF signal overlaid in false color on catheter outer surface. The bottom row shows the z-θ map of AF signal constructed over the entire pullback length. Each B-Scan in Fig. 4 and Fig. 5 contains 4032 A-lines.

Figure 4(a) shows results obtained from two fingers holding the distal end of the catheter. The AF map (bottom image) clearly shows the AF signal due to the fingerprints in great detail. The lower-intensity AF signal corresponding to the fingerprint valleys may be attributed to geometrical effects owing to the fact that the valleys have an oblique air-tissue interface, leading to more reflection and less transmission of blue AF excitation into the tissue. Also the AF collection efficiency decreases as the catheter-tissue distance increases. Figure 4(b) illustrates images from human oral cavity. The AF map (bottom) shows a strong AF signal from the teeth. Figure 4(c) shows images from pig airways. There are distinctive patterns in the AF map (bottom). Higher AF signals correspond to the areas with higher fluorophore concentrations. Cartilage and dense connective tissue include high concentrations of highly fluorescing collagen and elastin fibers [43]. Therefore, we expect that the regions with strong AF signal include cartilage and dense connective tissue. Strictly speaking, however, the scattering and absorption of superficial layers affect the AF signal measured at the luminal surface [10]. Therefore, more comprehensive studies are required to interpret AF images and to relate them to the fluorescing airway components in conjunction with the scattering and absorption effects of superficial layers.

#214233 - $15.00 USD Received 20 Jun 2014; revised 31 Jul 2014; accepted 1 Aug 2014; published 6 Aug 2014

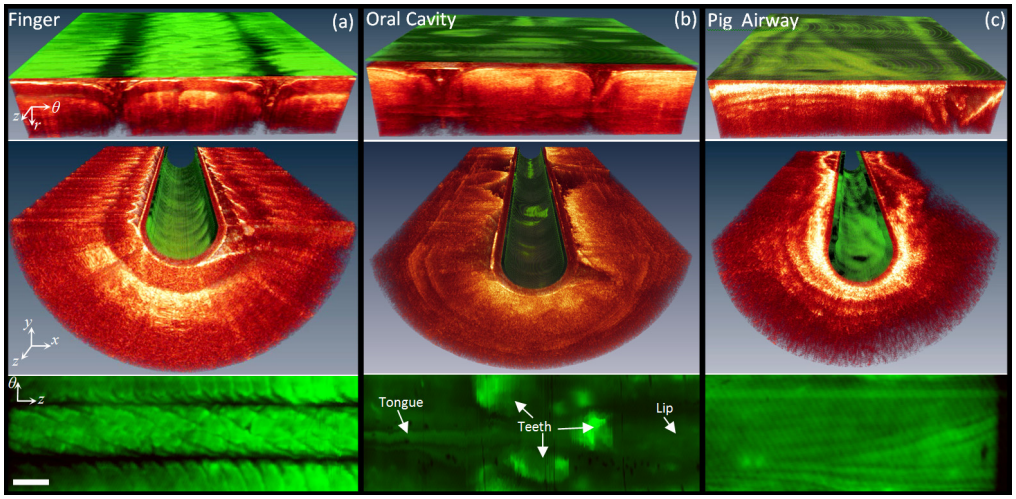

Fig. 4. AF/OCT imaging results; Volumetric AF/OCT images in polar (top row) and Cartesian (middle row) coordinates and the AF maps of (bottom row) (a) human finger pads and (b) oral cavity *in vivo*, and (c) porcine airway *ex vivo*. White bar is 1 mm.

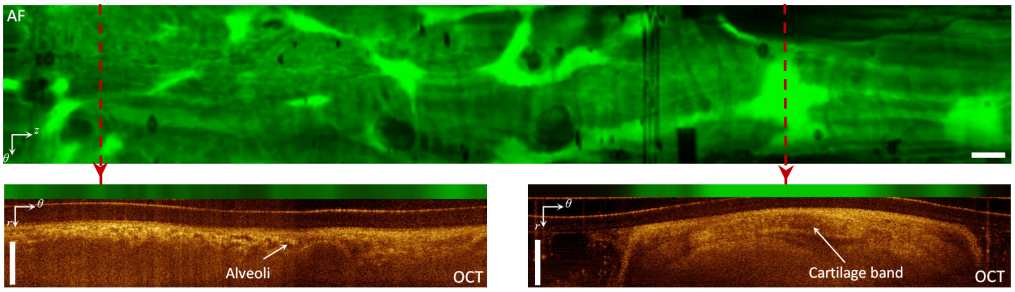

Fig. 5. AF/OCT imaging of human airway *in vivo*; top panel: AF map of human airway obtained from AF/OCT imaging *in vivo*; bottom panels: the AF/OCT images from two positions along the pullback axis specified with the dashed red lines on the AF map. White bar is 1 mm.

Figure 5 shows AF/OCT imaging from human airways acquired *in vivo*. The top panel shows the *en-face* AF *z*-θ map. AF/OCT images from two positions indicated along the pullback axis are shown in the bottom panels of the figure. Alveoli (small signal-void areas) are visible in the OCT cross-section at the distal end of the airway (left side of the AF map) while cartilage bands (larger structures with bright borders) are visible in the OCT cross-section at the proximal end of the airway (right side of AF map). The pattern of AF signal at the distal end of the AF map is clearly different from that of the proximal end. The strong AF signal on the right of the AF map due to the cartilage band just under the luminal surface confirms that cartilage produces larger autofluorescence signal. This is consistent with the results on *ex vivo* human airway sections presented in [43].

The AF signal from the airway components represents the fluorophore content of the components that, in turn, are related to the density of collagen and elastin fibers present in the tissue. The biochemical information from the AF signal co-localized with the structural information obtained from OCT may be used to better understand the pathogenesis of lung cancer. Following the changes in AF signal of the different airway tissue components during early cancer development may potentially provide useful information about processes involved in early cancer. Given the endoscopic co-registered AF/OCT imaging capability, we expect that the presented imaging system will become a useful tool in pulmonary medicine.

#214233 - $15.00 USD Received 20 Jun 2014; revised 31 Jul 2014; accepted 1 Aug 2014; published 6 Aug 2014

4. Conclusion

In this work, we present a power-efficient, fiber-based, dual-modality, AF/OCT imaging system for imaging airways *in vivo*. In this system, two imaging modalities are combined using a custom AF/OCT FORJ with lower insertion loss for the AF pathway compared to previously reported fiber-based approaches. A 900-µm DCF-based catheter enables *in vivo* imaging of small peripheral airways. Providing biochemical information about tissue co-localized with structural information, this system may be useful in clinical applications for monitoring changes in tissue associated with disease processes or therapeutic treatments in the lung or other organs.

Acknowledgment

This work was supported through grants from the Natural Sciences and Engineering Research Council of Canada (NSERC) and Canadian Institutes of Health Research (CIHR). The Michael Smith Foundation for Health and Research (MSFHR), NSERC, and Lotte & John Hecht Memorial Foundation provided Postdoctoral fellowships for HP.

#214233 - $15.00 USD Received 20 Jun 2014; revised 31 Jul 2014; accepted 1 Aug 2014; published 6 Aug 2014